Chip-scale Full-Stokes Spectropolarimeter in Silicon Photonic Circuits

Zhongjin Lin, Tigran Dadalyan, Simon Bélanger-de Villers, Tigran Galstian, and Wei Shi

OSA Photonics Research, (Volume 8, Issue 6) (2020)

Doi: 10.1364/PRJ.385008

https://doi.org/10.1364/PRJ.385008

Chip-scale Full-Stokes Spectropolarimeter in Silicon Photonic Circuits

ZHONGJIN LIN, TIGRAN DADALYAN, SIMON BÉLANGER-DE VILLERS, TIGRAN GALSTIAN AND WEI SHI*

Department of Electrical and Computer Engineering, Centre for Optics, Photonics and Laser (COPL), Université Laval, Québec, QC G1V 0A6, Canada
**wei.shi@gel.ulaval.ca*

Abstract: Wavelength-dependent polarization state of light carries crucial information about light-matter interactions. However, its measurement is limited to bulky, high energy-consuming devices, which prohibits many modern, portable applications. Here, we propose and demonstrate a chip-scale spectropolarimeter implemented using a complementary metal oxide semiconductor (CMOS) compatible silicon photonics technology. Four compact Vernier microresonator spectrometers are monolithically integrated with a broadband polarimeter consisting of a 2D nanophotonic antenna and a polarimetric circuit to achieve full-Stokes spectropolarimetric analysis. The proposed device offers a solid-state spectropolarimetry solution with a small footprint of 1×0.6 mm^2 and low power consumption of 360 mW. Full-Stokes spectral detection across a broad spectral range of 50 nm with a resolution of 1 nm is demonstrated in characterizing a material possessing structural chirality. The proposed device may enable a broader application of spectropolarimetry in the fields ranging from biomedical diagnostics and chemical analysis to observational astronomy.

1. Introduction

Monitoring the spectrum and polarization state of light can provide key information about light-matter interactions, revealing nanostructures of a material [1] and its chemical composition [2]. Measurement of wavelength-dependent state of polarization (*i.e.*, Stokes spectrum) is required for the studies of vibrational circular dichroism [3,4], Rayleigh scattering [5], vector magnetograph [6], and so on. A spectropolarimeter is used to measure the Stokes spectrum in these applications, which, in some fields, is also called spectroscopic ellipsometer [7]. Among other applications, such devices play a critical role in the pharmaceutical industry for chiral separation and analysis of racemic drugs: many drugs are chiral compounds and marketed as racemates, whose chirality can be measured via circular dichroism [8].

Over the last decade, the demand for compact, cost-effective, and low-power spectropolarimeters has increased dramatically. Recently, some miniature architectures of such devices have been demonstrated [9–12]. However, these works were still exploring the possible improvements of traditional free-space optical components. Not surprisingly, this approach is limited to the decimeter scale footprint. A new paradigm is needed to reach qualitative changes. A chip-scale spectropolarimeter would be highly desired (particularly for portable, biomedical applications), which has yet to be reported. In this work, we will propose a chip-level spectropolarimeter in silicon photonic integrated circuits (PICs).

The proposed device includes four spectrometers and one polarimeter. Some high-performance on-chip spectrometers have recently been demonstrated on silicon PICs, such as Fourier transform spectrometer (FTS) [13, 14] and arrayed-waveguide grating spectrometer (AWGS) [15]. The silicon FTS typically consumes a significant power (at the watt scale [13, 14]) for the thermal tuning of waveguide delay. Such a high power raises concerns about reliability and scalability for a lab-on-a-chip system. The power consumption of AWGS is relatively low, but requires a

National Science and Engineering Research Council of Canada (NSERC) Funding: STPGP 494358-16

large number of photodetectors, which complicates the measurement system and takes a large footprint [16]. The silicon FTS using arrayed Mach-Zehnder interferometers (MZIs) [17, 18] also has such a problem. The recently demonstrated digital silicon FTS using arrayed MZIs plus an on-chip thermo-optic switch fabric achieved a single photodetector solution with a lower power consumption, but at the cost of a larger footprint and increased control complexity [19].

Here, we will propose a structure of serially coupled double microring resonator (SDMR) to realize the chip-level spectrometer. With the advantages of small size, high tunability, and low-power consumption, microrings (MRs) is an excellent choice for wavelength filter [20]. But, the inverse relationship between the size and free spectral range (FSR) limits its application in spectroscopy. The structure of SDMR can well solve this problem. Because of the Vernier effect, the FSR of the SDMR can be significantly extended without decreasing the diameter of the MRs. More importantly, the temperature required to cover the entire FSR can be drastically reduced.

Compared to spectrometers, integrated polarimeters have been much less investigated. Only a few miniature full-Stokes polarimeters were demonstrated recently [9, 21–27]. The capacity of on-chip probing another dimension of photons than intensity and phase opened up immense opportunities for communications, quantum information, astronomy, and biomedical and chemical sensing. Our recent work [28] has proven that an optimal polarimetric frame with a minimum number of photodetectors can be achieved in silicon PICs, offering excellent performance comparable to conventional free-space solutions but with significantly improved compactness and robustness. Nevertheless, despite their broadband operation, none of these integrated polarimeters can capture the wavelength dependence of Stokes parameters.

In this paper, we propose and experimentally demonstrate, for the first time, a chip-scale spectropolarimeter in silicon PICs, which encompasses both functionalities of a full-Stokes polarimeter and four spectrometers. Analysis of an arbitrary state of polarization is realized using a 2D nanophotonic antenna and an on-chip interferometric circuit. With adopting SDMR, the proposed device simultaneously achieve a high resolution (1 nm) and a broad bandwidth (50 nm) in the Stokes spectrum. The efficacy of the proposed spectropolarimeter is demonstrated by characterizing the chirality of a cholesteric liquid crystal (CLC) slab. The whole device, including an array of photodetectors integrated on the same chip, takes a compact footprint of 0.6 mm^2 and a mean power consumption of only 360 mW.

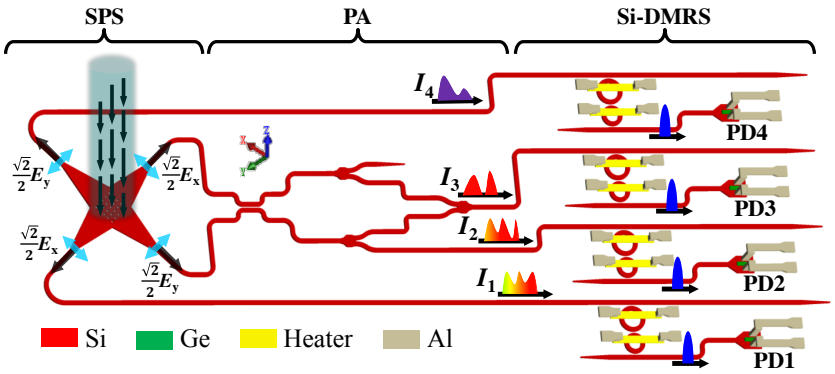

Fig. 1. Schematic of the proposed spectropolarimeter. The black arrows point to the propagating direction of light. SPS: surface polarization splitter; PA: polarization analyzer; Si-DMRS: our silicon dual-microring resonator sepectrometer; PDi: Ge photodetector of the i^{th} Si-DMRS.

National Science and Engineering Research Council of Canada (NSERC) Funding: STPGP 494358-16

2. Principle and design

Figure 1 shows a schematic of the proposed device. It is designed based on a standard 220-nm-thick silicon-on-insulator (SOI) wafer with a 2 μm buried oxide layer and 3 μm oxide cladding. A surface polarization splitter (SPS) is used to split an arbitrary state of polarization into two orthogonal linearly polarized components (E_x and E_y) and couple them into difference waveguides. A polarization analyzer (PA) in an interferometric circuit then converts the two orthogonal E-field components into four intensity channels. The spectrum of each intensity channel is measured using a chip-level spectrometer. The four spectral measurements capture the full information of wavelength-dependent polarization, from which we can eventually retrieve the Stokes spectra of the input light via an matrix operation.

The SPS makes use of a nanoantenna structure, consisting of a 2D array of sub-wavelength cylindrical holes on a Si substrate. The nanoantenna is designed so that both orthogonal linearly polarized components of the light, either from an optical fiber or free space, are coupled into the fundamental TE mode of the planar waveguides. Simultaneously, the SPS decomposes each orthogonal component equally into two paths in opposite directions as shown in Fig. 1.

The PA circuit consists of a 3-dB broadband directional coupler (BDC) [29], three Y-junctions [30] for 3-dB power splitting/combination, and a few delay lines. Taking the outputs of the SPS, the PA projects the Stokes vector of the incoming light into four intensity channels through interference operation: I_1 and I_4 from direct detection of $\frac{\sqrt{2}}{2}E_x$ and $\frac{\sqrt{2}}{2}E_y$, respectively; I_2 from the interference between $\frac{i\sqrt{2}}{4}E_x$ and $\frac{\sqrt{2}}{4}E_y$; I_3 from the interference between $\frac{1+i}{4}E_x$ and $\frac{1+i}{4}E_y$. Here, we denote the incoming polarization by a wavelength (λ) dependent Stokes vector: $\mathbf{S}(\lambda) = (S_0(\lambda), S_1(\lambda), S_2(\lambda), S_3(\lambda))^T$, where $(\star)^T$ means the transpose of the matrix $(\star)$. Defining a wavelength-dependent intensity vector: $\mathbf{I}(\lambda) = (I_1(\lambda), I_2(\lambda), I_3(\lambda), I_4(\lambda))^T$, we find the relationship between $\mathbf{I}(\lambda)$ and $\mathbf{S}(\lambda)$ given by,

$$\mathbf{S}(\lambda) \propto \mathbf{M_S}(\lambda) \cdot \mathbf{I}(\lambda) \tag{1}$$

where $\mathbf{M_S}(\lambda)$ is the synthesis matrix of the PA. The BDC [29] used in our design has a wide bandwidth in excess of 100 nm. Thus the synthesis matrix $\mathbf{M_S}(\lambda)$ is practically wavelength insensitive in the spectral range considered in this work and can be written by the following expression,

$$\mathbf{M_S}(\lambda) = 2\begin{pmatrix} 1 & 0 & 0 & 1 \\ 1 & 0 & 0 & -1 \\ -1 & 0 & 4 & -1 \\ -1 & 4 & 0 & -1 \end{pmatrix}. \tag{2}$$

Following the PA circuit, four silicon dual-microring resonator sepectrometers (Si-DMRSs) are used to measure the spectra of four intensity channels, respectively. Each Si-DMRS consists of an SDMR and a germanium on silicon photodetector (Ge-PD). The MRs in the SDMR have slightly different FSRs. Because of the Vernier effect, as shown in Fig. 2, the cascaded architecture can achieve a largely extended FSR without using ultra-small MRs which are challenging for fabrication on a wafer scale. The extended FSR of the SDMR is given by [31],

$$\mathrm{FSR} = \frac{\mathrm{FSR}_1 \cdot \mathrm{FSR}_2}{|\mathrm{FSR}_1 - \mathrm{FSR}_2|} = \frac{\lambda^2}{\pi|D_1 n_{g2} - D_2 n_{g1}|} \approx \frac{\lambda^2}{\pi n_{g1}|D_1 - D_2|} \tag{3}$$

where $\mathrm{FSR}_{1(2)}$, $D_{1(2)}$, and $n_{g1(2)}$ are the FSR, diameter, and group index of the single MRs, respectively; the subscript 1(2) indicates the first (second) MR. We have $n_{g1} \approx n_{g2}$ when the diameters of the two rings are very close. According to Eq. 3, we can increase the extended FSR

National Science and Engineering Research Council of Canada (NSERC) Funding: STPGP 494358-16

of the SDMR by decreasing the difference of the diameters. A metal heater is used on the top of each MR to individually vary their temperatures. Tuning the heating powers (HPs) applied to the MRs, the wavelength of each intensity channel, $I_i(\lambda)$, can be continuously swept and then detected by a Ge-PD. More details about the design of the SDMR are shown in **Appendix A**.

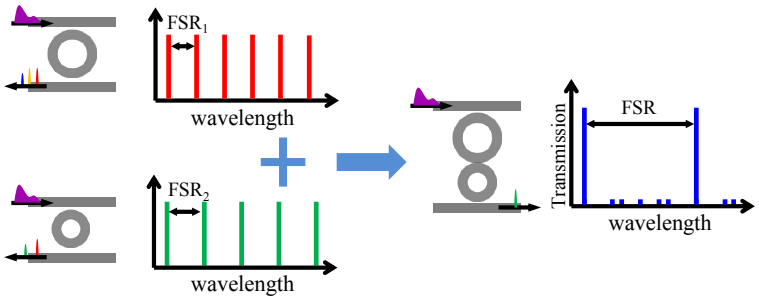

Fig. 2. Principle of the proposed Si-DMRS. $FSR_{1(2)}$ in the left side is the free spectral range of the single microring; the subscript 1(2) indicates the first (second) microring of the SDMR. FSR in the right side is the extended free spectral range of the SDMR.

3. Prototype

Figure 3(a) presents a packaged prototype of the proposed SP. Details of the fabrication and packaging processes are described in **Appendix D**. The fabricated silicon photonic chip sits in the center of the printed circuit board (PCB). Its footprint is $\sim 1 \times 0.6$ mm^2. The optical micrograph of the fabricated chip is depicted in Fig. 3(b). The footprint of each Ge-PD on the end of the right side is only 30 μm $\times$150 μm. The chip includes 16 electric I/O ports. The connections between these I/O ports are presented in **Appendix B**. Figure 3(c)-(e) present the scanning electron microscope (SEM) images of the SPS, BDC, and SDMR (silicon layer only), respectively. The effective area of the SPS for optical coupling is near 22 μm $\times$ 22 μm, which can be adjusted by varying the number of grating periods. More details about the design and performance of the SPS are given in **Appendix A**. The mean period and diameter of the holes of the fabricated SPS are 558 nm and 345 nm, respectively, which agree well with the designed parameters. The diameters of the two MRs in each SDMR are 26 μm (MR1) and 22 μm (MR2), respectively.

4. Result

4.1. Si-DMRS performance

Before our experiment with the full-Stokes spectrometer, we firstly characterized a single Si-DMRS integrated with a Ge-PD on the same chip. Figure 4(a) shows the optical micrography of the fabricated Si-DMRS. A Ge-PD design without doped Ge or Ge-metal contacts [32] was adopted in our device. Because the germanium lattice is not disturbed by dopants or metal contacts, it allows for better performance in background loss, bandwidth, and dark current. The Ge-PD was measured to have a responsivity of 1.12 A/W and dark current of ~15 nA at -4 V reverse bias, at 1550 nm wavelength. More information on the structure and performance of the Ge-PD is provided in **Appendix A**. Figure 4(b) shows the transmission spectrum from the drop port of the fabricated SDMR with a resonance wavelength near 1561 nm. A bimodal filter shape is observed and its 20-dB linewidth is near 0.9 nm. A sweeping step of 1 nm was chosen in the following experiment. An extended FSR of 50 nm is measured in Fig. 4(c).

The center wavelength as a function of HPs applied to MR1 and MR2 were calibrated for each channel using a tunable laser. More experimental details about the calibration are provided in

National Science and Engineering Research Council of Canada (NSERC) Funding: STPGP 494358-16

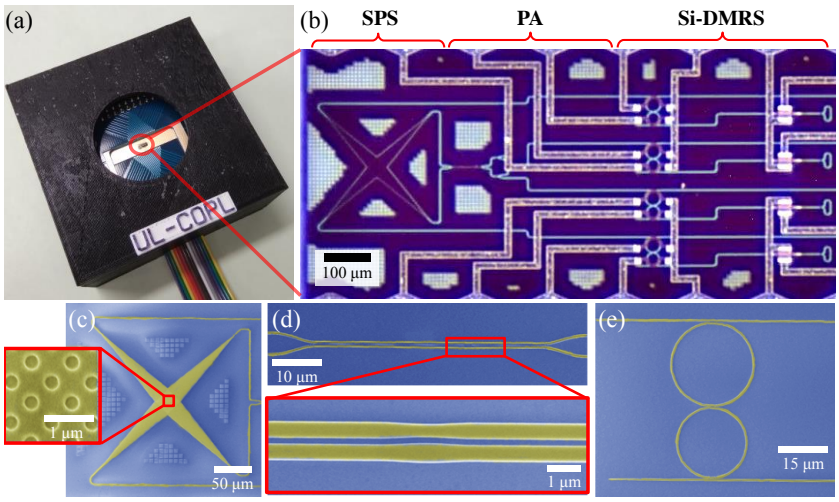

Fig. 3. Image of the fabricated spectropolarimeter. (a) the prototype of the fully packaged, plug-and-play spectropolarimeter with a ribbon cable for control and signal read-out. (b) The optical micrograph of the fabricated chip before being packaged. (c), (d) and (e) are the SEM images of the Si layer of the SPS, BDC, and SDMR, respectively. The inset in (d) presents the asymmetric-waveguide-based phase control section of the BDC for a broadband operation. SPS: surface polarization splitter; PA: polarization analyzer; Si-DMRS: our silicon dual-microring resonator sepectrometer.

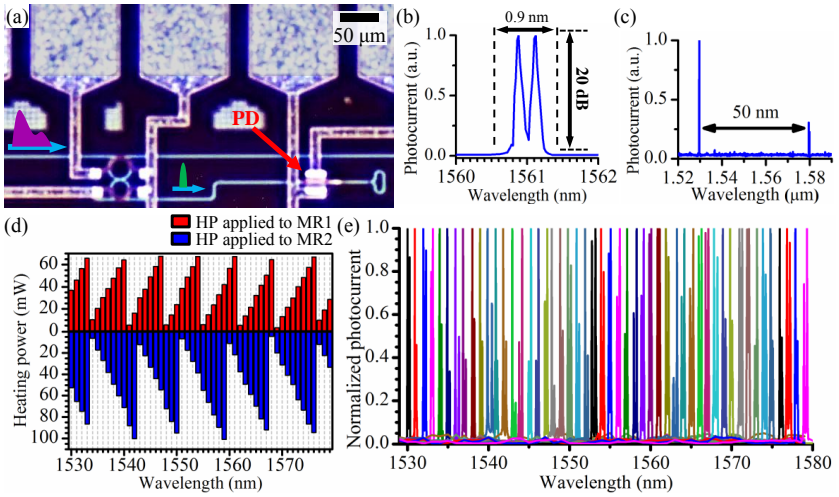

Fig. 4. Dual-MR characterization. (a) Optical micrography of a Si-DMRS. (b) and (c) The experimental transmission spectra from the drop port of the SDMR. (d) Relation between resonance wavelength and heating power on the heaters of MR1 (red dot) and MR2 (blue square). (e) The experimental transmission spectra of the drop port for the resonance wavelength from 1530 nm to 1579 nm.

Appendix B. The calibration result is shown in Fig. 4(d). The tuning efficiency is ~10 mW/nm and ~11 mW/nm for MR1 and MR2, respectively. Thanks to the Vernier effect, the maximum HPs required to cover the entire extended FSR for MR1 and MR2 are only ~70 mW and ~100 mW, respectively. Figure 4(e) shows the measured transmission spectra of the Si-DMRS swept across

National Science and Engineering Research Council of Canada (NSERC) Funding: STPGP 494358-16

the entire extended FSR (1530 nm to 1579 nm) with a step of 1 nm.

Figure 5 compares the spectrum of a broadband source recorded by a commercial optical spectrum analyzer (OSA) as a reference (solid black) and that measured by the Si-DMRS (dotted lines), where a good agreement is observed. To verify the stability of the proposed device, we perform several measurements within a week using the same HP calibration; results are shown in Fig. 4(d). The measurement results show excellent agreement over six day, indicating a very stable operation of our device. The measurement mean squared error between our device and reference is only 0.03.

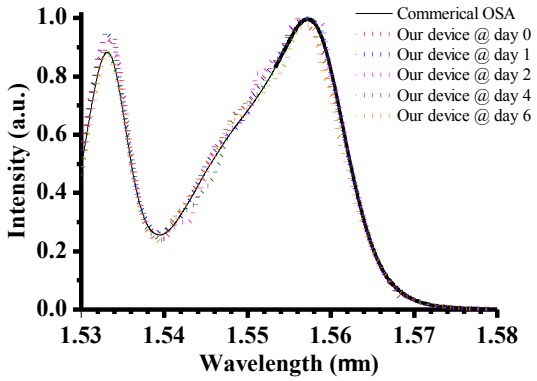

Fig. 5. Broadband spectrum reconstruction with the Si-DMRS. Solid black line is the spectrum recorded by a commerical OSA. The dotted lines are the measured results of the Si-DMRS over a week using the same calibration.

4.2. Spectropolarimetric characterization of a chiral material

The spectropolarimeter's performance was tested using a CLC slab [33]. The schematic of the CLC slab is presented in Fig. 6(a). It consists of chiral molecules with a mechanical twisting power, which imposes a macroscopic helicoidal self-organization. As a result, the local average orientation of long molecular axis is periodically rotating from layer to layer, forming a natural molecular helix (*i.e.*, structural chirality). With a proper choice of the molecular mixture parameters, the CLC slab acts like a spectral resonant filter (*e.g.*, Rocking filter) in a desired spectral range, which only left-handed (or right-handed) circular polarization can pass through. The most complex behavior occurs at the edges of the resonant wavelength range where polarization sensitive reflection and strong polarization rotations (along with strong dispersion) are present. To demonstrate the efficacy of the proposed spectropolarimeter, we fabricated a CLC sample with an edge of the resonant range near 1550 nm. More details about the fabrication of CLC sample are given in **Appendix C**.

With a linear polarization input (i.e.,$S_1/S_0 = 1$), the Stokes spectra of the CLC sample were measured by both a bench-top instrument and our device. Details about our experimental setup are provided in **Appendix B**. All the four Si-DMRSs were calibrated following the procedure described in **Appendix B**. The calibration results are depicted in Fig.12 of **Appendix B**. The wavelength dependent synthesis matrix of the PA, $\mathbf{M_s}(\lambda)$, was calibrated using four known independent polarization states.

Figure 6(b) shows the measured normalized Stokes parameters S_1/S_0, S_2/S_0, and S_3/S_0 obtained by a bench-top instrument (dotted line) and our device (solid line). Excellent agreement is observed in the measurement results between our device (solid lines) and a bench-top instrument (dotted lines). The resonant range of the fabricated CLC material is below 1.52 μm. In the resonant range, only left-handed circular polarization can pass through the CLC; as shown in

National Science and Engineering Research Council of Canada (NSERC) Funding: STPGP 494358-16

Figure 6(b), S_3/S_0 evolves towards -1, while S_1/S_0 and S_2/S_0 approaches zero as wavelength decreases. While in the non-resonant range (beyond 1.58 μm), the CLC material does not change the input polarization state. Therefore, as seen in Fig. 6(b), S_1/S_0 increases gradually from 0 towards 1 with the wavelength, while S_3/S_0 increases from -1 to 0 in the non-resonant range.

Compared to the bench-top instrument, our device shows a mean squared error of 0.04 in polarization measurement (Fig. 6(b)). It can be reduced by: 1) optimizing the architecture of the PA, e.g., a broadband optimal PA was recently proposed [34]; 2) improving the thermal stability of the SDMR, which limits the accuracy of our spectrometer; 3) reducing the noise of the on-chip Ge-PD.

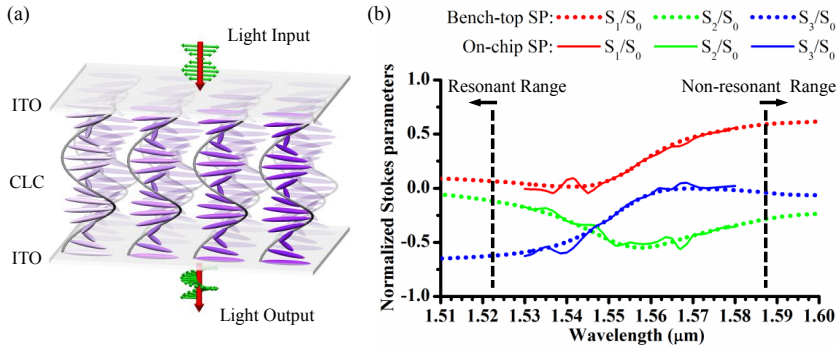

Fig. 6. On-chip spectropolarimeter characterization: (a) schematic of the CLC sample. (b) Normalized Stokes spectra of the CLC sample, with a linear polarization input, measured by a commercial bench-top instrument (dotted lines) and our on-chip spectropolarimeter (solid lines).

5. Discussion

The entire spectropolarimeter, consisting of an SPS, a PA, and four spectrometers with Ge-PDs, has a compact footprint of $\sim 1 \times 0.6$ mm^2. In spite of compactness, our device remains a high performance with a high resolution (1 nm) and broad bandwidth (50 nm) of Stokes spectrum, which, however, has still not reached its limits. For example, according to Eq. 3, we can obtain a bandwidth of 100 nm if increasing the diameter of MR_2 to 24 μm. Besides, the spectral resolution of the proposed device can be further improved by another order of magnitude (to 0.1 nm) by decreasing the cross-coupling coefficient between the two MRs without introducing significant losses (as shown in **Appendix B**). Other solutions for resolution improvement include the use of an integrated Fabry-Perot cavity [35]. The performance of PA can also be improved by adopting the optimal measurement frame as shown in our previous analysis [28]. However, increasing the number of measurement channels does not necessarily improve the performance because it reduces the power received by individual channels and thus the signal to noise ratio. With a proper design, an optimal performance can be achieved with four measurement channels, the minimum required for the reconstruction of full-Stokes vectors, in the presence of both additive Gaussian noise and shot noise [28].

Because of the employment of the Si-DMRS, the energy consumption is significantly reduced. Our spectropolarimeter only dissipates near 3.6 J of energy to complete one measurement of the Stokes spectra, a few orders of magnitude lower than traditional solutions. The tuning efficiency can be further improved by adding thermal isolation trenches near the MRs (> 10 times) [36] and by increasing the sweeping frequency of the HP (> 100 times). Due to the limitation of our set-up, the sweeping frequency was only 5 Hz in our experiment. However, the thermal response time of the MR is lower than 4 μs, indicating that a sweeping frequency of 250 kHz

National Science and Engineering Research Council of Canada (NSERC) Funding: STPGP 494358-16

is possible [37], which can also be improved by applying micro-heaters embedded in silicon waveguides [38]. Assuming a higher sweeping frequency of 5 kHz for a larger number of spectral sweeping steps of 1,000 (versus 50 in our current experiment), the total energy consumption of the proposed spectropolarimeter is estimated to be only ~72 mJ. In this case, one measurement of Stokes spectra can be accomplished within 0.2 s.

The resonance wavelength of our SDMR is sensitive to the temperature. Thus, the thermal stability determines the wavelength accuracy, which can be understood by the relation between the wavelength drift ($\Delta\lambda$) of the spectrometer and the local temperature deviation (ΔT) :

$$\Delta\lambda = \frac{\lambda_0}{n_g(\lambda_0, T_0)} \cdot \left(\frac{\partial n_{eff}(\lambda_0, T_0)}{\partial T} + \alpha_L \right) \cdot \Delta T \tag{4}$$

where $n_{eff}(\lambda_0, T_0)$ and $n_g(\lambda_0, T_0)$ are the effective and group index of the MR waveguide, respectively; λ_0 is the measured wavelength and T_0 is the local temperature of the MRM; α_L is the linear thermal expansion coefficient of waveguide. For example, assuming ΔT within ±0.1 °C, the wavelength accuracy is about 7 pm according to Eq. 4, which can meet requirements of most practical applications.

6. Conclusion

Achieving an integrated spectropolarimeter on a silicon photonic chip paves the way towards fast, affordable full-Stokes spectroscopy. To decrease the cost and size of the device, traditional solutions come with a reduced number of spectroscopic components, and consequently, compromised measurement speed and Stokes spectral resolution. By contrast, our solution allows for simultaneous achievement of a high speed and high resolution as all the Si-DMRSs can be monolithically integrated with little increase in footprint and cost. Our device is fabricated using industry-standard silicon photonics foundry processes, indicating an easier path towards mass production using established large-wafer manufacturing facilities. The operating frequency range can be readily extended to the visible and mid-infrared regions by using other complementary metal oxide semiconductor (CMOS) compatible material platforms (*e.g.*, silicon nitride-based platform and germanium-based platform) but the same architecture. Leveraging the economies of scale and advantages of silicon PICs integration, the proposed spectropolarimeter has a vast potential for application in the fields of Internet of Things, pharmaceutical analysis, astronomy, and so on. Moreover, an array of our devices can be used to analyze a light beam with complex spatial modes such as optical vortex [39].

7. Appendix A: Components

7.1. Surface polarization splitter

The schematic of surface polarization splitter (SPS) is shown in Fig. 7(a). The parameters Λ and D are the period and diameter of the holes, respectively [21]. It is formed using a 40 × 40 array of cylindrical holes shallowly etched through silicon with a depth of 70 nm. The characteristics of SPS depend on Λ and D. Λ= 562 nm and D = 360 nm have been chosen in our design. The design follows the same method given in our previous paper [21]. The simulation results of the proposed SPS are presented in Fig. 7(b), showing a coupling efficiency near -4 dB at 1550 nm. In our experiment, a lower coupling efficiency of about -15 dB was measured due to the large beam size of the optical input and the misalignment. In addition to improvement of the experimental setup, the coupling efficiency can be further enhanced by adding a backside metal mirror [40]. Note that the loss of the overall device is most caused by the SPS.

National Science and Engineering Research Council of Canada (NSERC) Funding: STPGP 494358-16

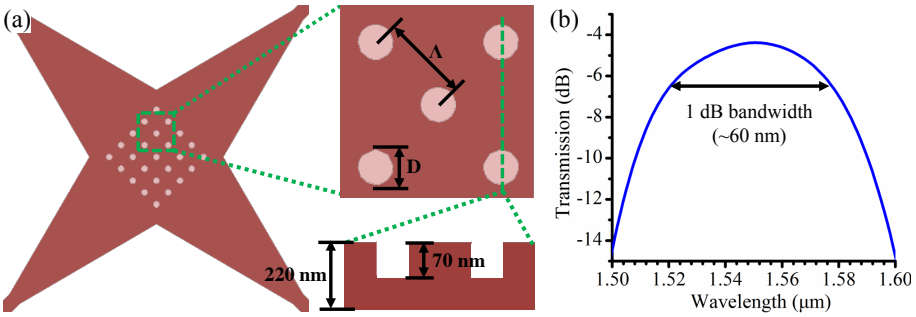

Fig. 7. (a) Schematic of SPS. The parameters Λ and D are the period and diameter of the hole, respectively. (b) The simulated transmission spectra of SPS.

7.2. Serially coupled double microring resonator

The schematic of the serially coupled double microring resonator (SDMR) is shown in Fig. 8(a). E_{in}, E_T, E_A, and E_D are the electrical fields in the input, through, add, and drop ports of the SDMR, respectively. The relation between $(E_{in},\ E_T)^T$ and $(E_A,\ E_D)^T$ can be written by [41],

$$\begin{pmatrix} E_A \\ E_D \end{pmatrix} = (\mathbf{C}_3\mathbf{P}_2\mathbf{C}_2\mathbf{P}_1\mathbf{C}_1)\begin{pmatrix} E_{in} \\ E_T \end{pmatrix} = \mathbf{M}\begin{pmatrix} E_{in} \\ E_T \end{pmatrix}. \tag{5}$$

where $\mathbf{C}_1$, $\mathbf{C}_2$, and $\mathbf{C}_3$ are the coupling matrices and can be given by,

$$\mathbf{C}_{1,(2,\ 3)} = \frac{i}{\kappa_{1,(2,\ 3)}}\begin{pmatrix} t_{1,(2,\ 3)} & -1 \\ 1 & t_{1,(2,\ 3)} \end{pmatrix} \tag{6}$$

where $i^2 = -1$. $t_{1,(2,\ 3)}$ and $\kappa_{1,(2,\ 3)}$ are the transmission and cross-coupling coefficients, respectively, assuming $|t_{1,(2,\ 3)}|^2 + |\kappa_{1,(2,\ 3)}|^2 = 1$. $\mathbf{P}_1$, $\mathbf{P}_2$ are the propagation matrices, and can be given by,

$$\mathbf{P}_{1,(2)} = \begin{pmatrix} 0 & \sqrt{\alpha_{1,(2)}}\exp\left(-i\pi\beta_{1,(2)}R_{1,(2)}\right) \\ \sqrt{\alpha_{1,(2)}}\exp\left(i\pi\beta_{1,(2)}R_{1,(2)}\right) & 0 \end{pmatrix} \tag{7}$$

where $\alpha_{1,(2)}$, $\beta_{1,(2)}$, and $R_{1,(2)}$ are the round trip attenuation, propagation constant, and radius of MR1(2), respectively. If we set $\mathbf{M}$ as,

$$\mathbf{M} = \begin{pmatrix} m_{11} & m_{12} \\ m_{21} & m_{22} \end{pmatrix} \tag{8}$$

, the normalized output intensities at the "drop" (E_D) port and "through" (E_T) port of the SDMR can be obtained by,

$$|E_D|^2 = |-\frac{\mathrm{Det}\,(\mathbf{M})}{m_{12}}|^2,\ |E_T|^2 = |-\frac{m_{11}}{m_{12}}|^2, \tag{9}$$

When R_1= 13 μm and R_2= 11 μm, $\kappa_1 \approx 0.125$ and $\kappa_3 \approx 0.115$. In this case, the spectra of the drop port as a function with the cross-coupling coefficient κ_2 are presented in Fig. 8(b). We can observe that the 20-dB linewidth of the SDMR decreases with reducing the cross-coupling coefficient κ_2. When $\kappa_2 = 0.005$, the 20-dB linewidth of the SDMR is equal to 0.2 nm, indicating a resolution of 0.1 nm is available. The spectral interval between the two split resonances change with κ_2 can be explained by the mode splitting [42, 43].

National Science and Engineering Research Council of Canada (NSERC) Funding: STPGP 494358-16

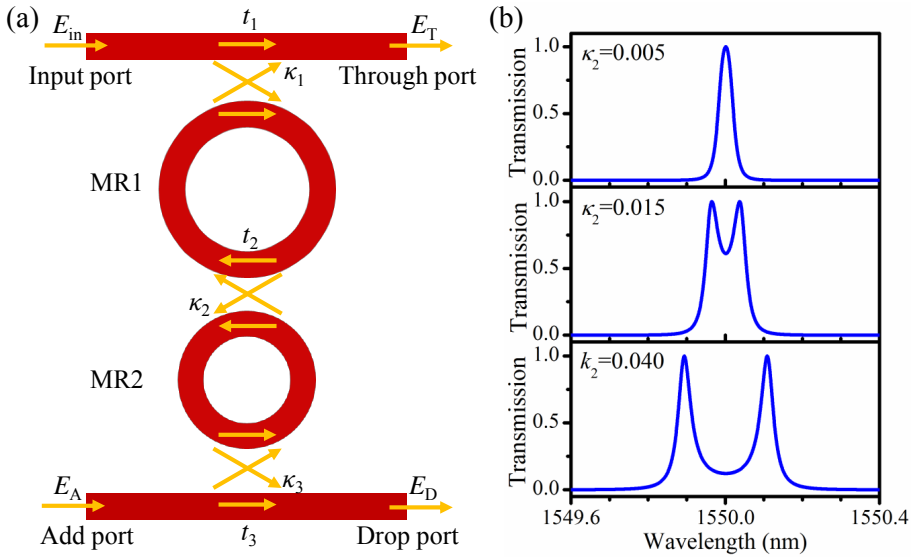

Fig. 8. (a) Schematic of SDMR. $t_{1,(2,3)}$ and $\kappa_{1,(2,3)}$ are normalized transmission and cross-coupling coefficients, respectively. (b) The simulated transmission spectra of the drop port in the case of κ_2 = 0.005, κ_2 = 0.015, and κ_2 = 0.04 when the resonant wavelength is near 1550 nm.

7.3. Ge-on-Si photodetector

The cross-sectional schematic of the Ge-PD is shown in Fig. 9(a). The experimental I-V curve in darkness is presented in Fig. 9(b). The breakdown voltage situates at -7 V. Figure 9(c) depicts the photocurrent of the Ge-PD as a function with the optical power when applying a bias voltage of -4 V. In this case, the responsivity and dark current of the Ge-PD are near 1.12 A/W and 10.8 nA, respectively.

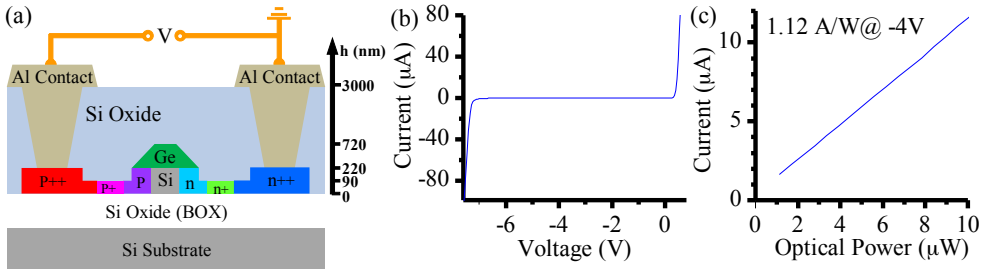

Fig. 9. (a) The cross-sectional schematic of the Ge-PD. (b) I-V curve in darkness. (c) Photocurrent as a function of optical power for the bias voltage of -4 V.

8. Appendix B: Experiment

8.1. Heating power calibration

In this section, we describe how to calibrate the heating powers for wavelength sweeping of the spectropolarimeter. The same method is applied to calibrate the single spectrometer. The electric connections of the device are illustrated in Fig. 10(a). Our device includes four SDMRs. Each SDMR consists of two microrings (marked as MR_{ij}, where i=1, 2, 3 and 4 indicate the 1st, 2nd,

National Science and Engineering Research Council of Canada (NSERC) Funding: STPGP 494358-16

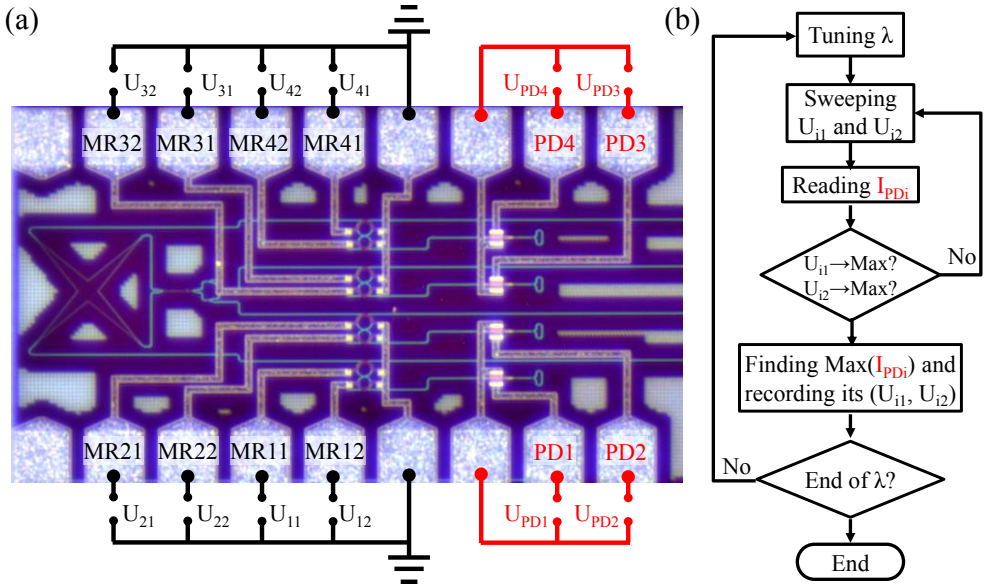

Fig. 10. (a) The schematic of the electric connections. (b) The flowchart of searching the corresponding (U_{i1}, U_{i2}) for each wavelength. U_{i1} and U_{i2} are the power applied to 1st and 2nd MRs of the i^{th} SDMR, respectively. PD_i means the photodtector of the i^{th} SDMR. I_{PDi} is the current read from the PD_i.

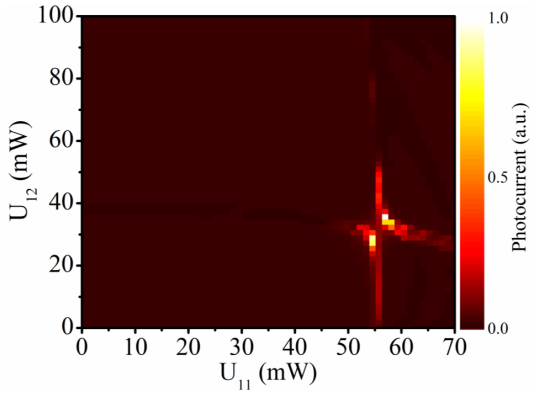

Fig. 11. The photocurrent as a function of U_{11} and U_{12} at a wavelength of 1562 nm.

3rd, and 4th SDMR, respectively; j=1 and 2 indicate the 1st and 2nd MRs of SDMR). Here, we define U_{i1} and U_{i2} as the power applied to 1st and 2nd MRs of the ith SDMR, respectively. PD_i means the photodtector of the ith SDMR. I_{PDi} is the current read from the PD_i. Fig. 10(b) presents the experimental flowchart that finding the corresponding (U_{i1}, U_{i2}) for each spectral channel:

(1) Set the input wavelength as 1530 nm by a tunable laser;

(2) Sweep the input power of U_{i1} and U_{i2} from 0 to 70 mW and from 0 to 100 mW, respectively. The size of the total points (U_{i1}, U_{i2}) is 71 × 101;

(3) For each (U_{i1}, U_{i2}), the photocurrent I_{PDi} is read;

(4) After all the permutations of U_{i1} and U_{i2} is swept, we find the maximum I_{PDi} and record the corresponding (U_{i1}, U_{i2}). Figure 11 is an example of I_{PD1} as a function of U_{11} and U_{12} when

National Science and Engineering Research Council of Canada (NSERC) Funding: STPGP 494358-16

the input wavelength is 1562 nm. Due to the mode splitting, two peaks are observed. We choose the peak with the lower heating powers.

(5) Increase the wavelength and sweeping the input power of U_{i1} and U_{i2} again until 1579 nm. The calibration results of the four SDMRs are shown in Fig. 12.

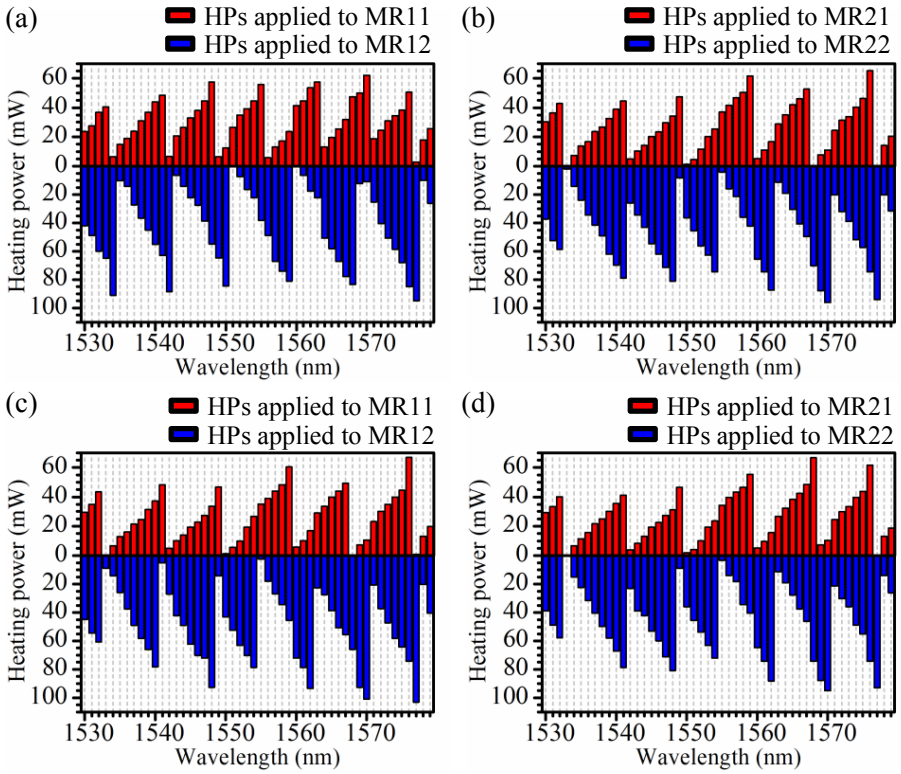

Fig. 12. (a)-(d) are the calibrated heating power of MRi1 (red) and MRi2 (blue) for each spectral channel.

8.2. Experiment setup

The experiment setup for calibrating the synthesis matrix or characterizing a chiral material is shown in Fig. 13. The input polarization is controlled by rotating the angles of the half-wave plate (HWP) and quarter-wave plate (QWP) and can be calculated by the angles of HWP and QWP. Therefore, we can calibrate the synthesis matrix of our device using HWP and QWP. If we want to measure the sample, we can replace the HWP and QWP by the sample.

9. Appendix C: Materials and methods

9.1. Device fabrication.

The device was fabricated by the Institute of Microelectronics (IME), Singapore, using a commercial CMOS-compatible SOI process with 193 nm deep-UV lithography. More details about the optical component of our device can be found in Section 7. The devices were subsequently packaged at our lab. The electrical connections were realized using Westbond's 7400A Wire Bonder. The plastic cover shell was fabricated using a 3D printer (Ultimaker S5).

National Science and Engineering Research Council of Canada (NSERC) Funding: STPGP 494358-16

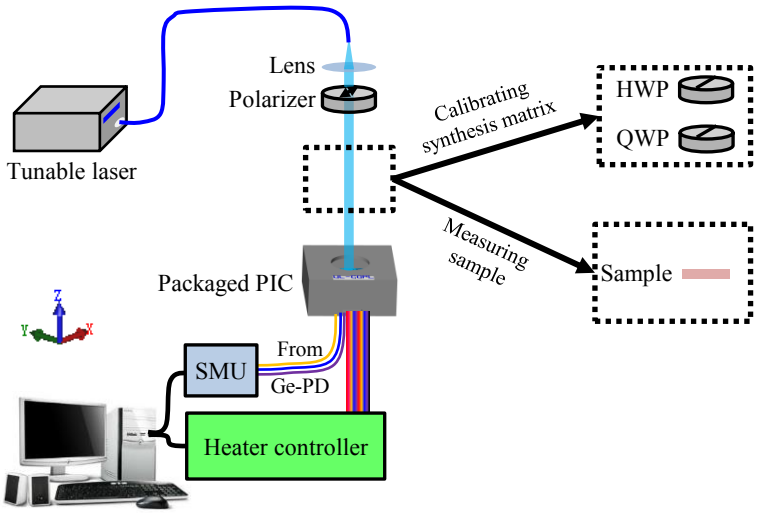

Fig. 13. Experiment setup for calibrating the synthesis matrix or characterizing a chiral material. HWP: half-wave plate; QWP: quarter-wave plate. SMU: source measure unit used for reading the current from photodetector.

9.2. Chiral molecule sample fabrication.

The CLC material used was a mixture of commercially available Nematic Liquid Crystal (NLC) 20608 (Qingdao Chemicals) and the chiral molecule CB15 (Merck). We have adjusted their ratio (75:25 wt % ratio), so that we can obtained a CLC with selective reflection band in the near IR region. The CLC mixture was heated above the clearing point (isotropic phase transition) and filled into the LC cell of 9.6 μm thickness by capillary method and then was slowly cooled down to the room temperature. The cell consists of two indium tin oxide /ITO/ coated transparent glass substrates, which are coated with alignment layers that align CLC molecules parallel to the surface of the substrates.

9.3. Device characterization.

The calibration of the HP described in the main text was performed using a tunable laser source (Agilent 81600B) with optical power around 3 dBm. The photocurrents from Ge-PD were read by a Keithley 2612B souremeter. The HPs of the heaters were driven using a Keysight E3631A power supply. The light from a high-power wide-band Erbium ASE source (INO) was used to characterize the Si-DMRS. A commercial optical spectrum analyzer (OSA, Yokogawa AQ6370D) was used to measure its spectrum. The synthesis matrix of the proposed spectropolarimeter was calibrated by a polarizer (LPNIR100-MP2, Thorlabs), an HWP (WPH10M-1550, Thorlabs), and a QWP (WPQ10M-1550, Thorlabs). Two stepper motor rotators (K10CR1/M, Thorlabs) were used to control separately the angles of the HWP and QWP.

10. Appendix D: Summary of recently demontrated spectropolarimeters

The state-of-art spectropolarimeters are summarized in Table 1.

Funding

Natural Sciences and Engineering Research Council (NSERC) of Canada (STPGP 494358 - 16)

Table 1. **Performance of recently demonstrated spectropolarimeters.**

Reference	[9, 44]	[10]	[45]	This paper
Material platform	Discrete components	Metasurface	Discrete components	Silicon Photonics
Bandwidth	450-700 nm	500-700 nm	450-650 nm	1530-1579 nm
Resolution	Not provided	25 nm	5.7 nm	1 nm
On-chip photodetection?	No	No	No	Yes
Error in azimuth*	0.01°	Not provided	Not provided	2.63°
Error in ellipticity*	0.01°	Not provided	Not provided	1.31°

* The spherical coordinates of the three-dimensional vector of Cartesian coordinates $(S_1/S_0, S_2/S_0, S_3/S_0)$ are used here to be consistent with the results reported in [9, 44]. In the main text, the mean squared error of (S_1/S_0, S_2/S_0, S_3/S_0) is reported in the Cartesian coordinates (0.04 in our case).

Acknowledgments

Zhongjin Lin would like to thank the support from the China Scholarship Council (NO. 201606890030). We thank Guan Xun for welding the electrical cable onto the PCB, and Jonathan St-Yves for the layout design of the photodetector. We also thank Simon Levasseur and Nathalie Bacon for their technical support.

Disclosures

The authors declare no conflicts of interest

References

1. M. Mishchenko and J. Hovenier, "Depolarization of light backscattered by randomly oriented nonspherical particles," Opt. letters **20**, 1356–1358 (1995).
2. D. Naumann, D. Helm, and H. Labischinski, "Microbiological characterizations by FT-IR spectroscopy." Nature **351**, 81–82 (1991).
3. U. D. Hemraz, M. El-Bakkari, T. Yamazaki, J.-Y. Cho, R. L. Beingessner, and H. Fenniri, "Chiromers: conformation-driven mirror-image supramolecular chirality isomerism identified in a new class of helical rosette nanotubes," Nanoscale **6**, 9421–9427 (2014).
4. J. Kessler, V. Andrushchenko, J. Kapitán, and P. Bouř, "Insight into vibrational circular dichroism of proteins by density functional modeling," Phys. Chem. Chem. Phys. **20**, 4926–4935 (2018).
5. R. Wehner, "Polarization vision–a uniform sensory capacity?" J. Exp. Biol. **204**, 2589–2596 (2001).
6. M. L. Degl'Innocenti and M. Landolfi, *Polarization in spectral lines*, vol. 307 (Springer Science & Business Media, 2006).
7. H. Fujiwara, *Spectroscopic ellipsometry: principles and applications* (John Wiley & Sons, 2007).
8. L. A. Nguyen, H. He, and C. Pham-Huy, "Chiral drugs: an overview," Int. journal biomedical science: IJBS **2**, 85 (2006).
9. A. Taniguchi, K. Oka, H. Okabe, H. Naito, and N. Nakatsuka, "Miniaturized channeled spectropolarimeter," in *2006 Conference on Lasers and Electro-Optics and 2006 Quantum Electronics and Laser Science Conference,* (IEEE, 2006), pp. 1–2.
10. W. T. Chen, P. Török, M. R. Foreman, C. Y. Liao, W.-Y. Tsai, P. R. Wu, and D. P. Tsai, "Integrated plasmonic metasurfaces for spectropolarimetry," Nanotechnology **27**, 224002 (2016).

National Science and Engineering Research Council of Canada (NSERC) Funding: STPGP 494358-16

11. H. Okabe, M. Hayakawa, J. Matoba, H. Naito, and K. Oka, "Error-reduced channeled spectroscopic ellipsometer with palm-size sensing head," Rev. Sci. Instruments **80**, 083104 (2009).
12. D. J. Lee, C. F. LaCasse, and J. M. Craven, "Compressed channeled spectropolarimetry," Opt. express **25**, 32041–32063 (2017).
13. S. Zheng, J. Zou, H. Cai, J. Song, L. Chin, P. Liu, Z. Lin, D. Kwong, and A. Liu, "Microring resonator-assisted Fourier transform spectrometer with enhanced resolution and large bandwidth in single chip solution," Nat. communications **10**, 2349 (2019).
14. M. C. Souza, A. Grieco, N. C. Frateschi, and Y. Fainman, "Fourier transform spectrometer on silicon with thermo-optic non-linearity and dispersion correction," Nat. communications **9**, 665 (2018).
15. H. Takahashi, S. Suzuki, K. Kato, and I. Nishi, "Arrayed-waveguide grating for wavelength division multi/demultiplexer with nanometre resolution," Electron. letters **26**, 87–88 (1990).
16. P. Cheben, J. Schmid, A. Delâge, A. Densmore, S. Janz, B. Lamontagne, J. Lapointe, E. Post, P. Waldron, and D.-X. Xu, "A high-resolution silicon-on-insulator arrayed waveguide grating microspectrometer with sub-micrometer aperture waveguides," Opt. express **15**, 2299–2306 (2007).
17. H. Wang, Z. Lin, Q. Li, and W. Shi, "On-chip fourier transform spectrometers by dual-polarized detection," Opt. Lett. **44**, 2923–2926 (2019).
18. A. V. Velasco, P. Cheben, P. J. Bock, A. Delâge, J. H. Schmid, J. Lapointe, S. Janz, M. L. Calvo, D.-X. Xu, M. Florjańczyk, and M. Vachon, "High-resolution Fourier-transform spectrometer chip with microphotonic silicon spiral waveguides," Opt. letters **38**, 706–708 (2013).
19. D. M. Kita, B. Miranda, D. Favela, D. Bono, J. Michon, H. Lin, T. Gu, and J. Hu, "High-performance and scalable on-chip digital fourier transform spectroscopy," Nat. communications **9**, 4405 (2018).
20. Z. Xia, A. A. Eftekhar, M. Soltani, B. Momeni, Q. Li, M. Chamanzar, S. Yegnanarayanan, and A. Adibi, "High resolution on-chip spectroscopy based on miniaturized microdonut resonators," Opt. express **19**, 12356–12364 (2011).
21. Z. Lin, L. Rusch, Y. Chen, and W. Shi, "Chip-scale, full-Stokes polarimeter," Opt. express **27**, 4867–4877 (2019).
22. Z. Lin, Y. Chen, L. Rusch, and W. Shi, "On-chip circular polarization splitter using silicon photonic nanoantenna array," ACS Photonics **5**, 4338–4342 (2018).
23. W. Wu, Y. Yu, W. Liu, and X. Zhang, "Fully integrated CMOS-compatible polarization analyzer," Nanophotonics **8**, 467–474 (2019).
24. A. Espinosa-Soria, F. J. Rodríguez-Fortuño, A. Griol, and A. Martínez, "On-chip optimal Stokes nanopolarimetry based on spin–orbit interaction of light," Nano letters **17**, 3139–3144 (2017).
25. A. Martínez, "Polarimetry enabled by nanophotonics," Science **362**, 750–751 (2018).
26. J. B. Mueller, K. Leosson, and F. Capasso, "Ultracompact metasurface in-line polarimeter," Optica **3**, 42–47 (2016).
27. P. C. Wu, J.-W. Chen, C.-W. Yin, Y.-C. Lai, T. L. Chung, C. Y. Liao, B. H. Chen, K.-W. Lee, C.-J. Chuang, C.-M. Wang, and D. P. Tsai, "Visible metasurfaces for on-chip polarimetry," ACS Photonics **5**, 2568–2573 (2017).
28. Z. Lin, L. A. Rusch, Y. Chen, and W. Shi, "Optimal ultra-miniature polarimeters in silicon photonic integrated circuits," APL Photonics **4**, 100806 (2019).
29. Z. Lu, H. Yun, Y. Wang, Z. Chen, F. Zhang, N. A. Jaeger, and L. Chrostowski, "Broadband silicon photonic directional coupler using asymmetric-waveguide based phase control," Opt. express **23**, 3795–3808 (2015).
30. Z. Lin and W. Shi, "Broadband, low-loss silicon photonic Y-junction with an arbitrary power splitting ratio," Opt. express **27**, 14338–14343 (2019).
31. V. R. Kolli, T. Srinivasulu, G. Hegde, T. Badrinarayana, and S. Talabattula, "Design and analysis of serially coupled double microring resonator based force sensor for 1 μN range measurement," Optik **131**, 1063–1070 (2017).
32. Y. Zhang, S. Yang, Y. Yang, M. Gould, N. Ophir, A. E.-J. Lim, G.-Q. Lo, P. Magill, K. Bergman, T. Baehr-Jones, and M. Hochberg, "A high-responsivity photodetector absent metal-germanium direct contact," Opt. express **22**, 11367–11375 (2014).
33. P.-G. De Gennes and J. Prost, *The physics of liquid crystals*, vol. 83 (Oxford university press, 1995).
34. Z. Lin and W. Shi, "Broadband silicon photonic polarimeter using subwavelength grating metamaterial waveguides," in *Smart Photonic and Optoelectronic Integrated Circuits XXII,* vol. 11284 (International Society for Optics and Photonics, 2020), p. 112841K.
35. J. Wu, T. Moein, X. Xu, G. Ren, A. Mitchell, and D. J. Moss, "Micro-ring resonator quality factor enhancement via an integrated Fabry-Perot cavity," Apl Photonics **2**, 056103 (2017).
36. P. Ying, R. Ge, S. Gao, and X. Cai, "Thermally tunable silicon microring resonators with ultralow tuning power," in *17th International Conference on Optical Communications and Networks (ICOCN2018),* vol. 11048 (International Society for Optics and Photonics, 2019), p. 1104839.
37. A. Atabaki, E. S. Hosseini, A. Eftekhar, S. Yegnanarayanan, and A. Adibi, "Optimization of metallic microheaters for high-speed reconfigurable silicon photonics," Opt. express **18**, 18312–18323 (2010).
38. L. Zhou, X. Zhang, L. Lu, and J. Chen, "Tunable vernier microring optical filters with $p-i-p$-type microheaters," IEEE Photonics J. **5**, 6601211–6601211 (2013).
39. N. Zhou, S. Zheng, X. Cao, Y. Zhao, S. Gao, Y. Zhu, M. He, X. Cai, and J. Wang, "Ultra-compact broadband polarization diversity orbital angular momentum generator with 3.6× 3.6 μm2 footprint," Sci. advances **5**, eaau9593 (2019).
40. W. S. Zaoui, M. F. Rosa, W. Vogel, M. Berroth, J. Butschke, and F. Letzkus, "Cost-effective CMOS-compatible

National Science and Engineering Research Council of Canada (NSERC) Funding: STPGP 494358-16

grating couplers with backside metal mirror and 69% coupling efficiency," Opt. express **20**, B238–B243 (2012).
41. S.-Y. Cho and R. Soref, "Interferometric microring-resonant 2× 2 optical switches," Opt. express **16**, 13304–13314 (2008).
42. J. Wu, B. Liu, J. Peng, J. Mao, X. Jiang, C. Qiu, C. Tremblay, and Y. Su, "On-chip tunable second-order differential-equation solver based on a silicon photonic mode-split microresonator," J. Light. Technol. **33**, 3542–3549 (2015).
43. X. Xue, Y. Xuan, P.-H. Wang, Y. Liu, D. E. Leaird, M. Qi, and A. M. Weiner, "Normal-dispersion microcombs enabled by controllable mode interactions," Laser & Photonics Rev. **9**, L23–L28 (2015).
44. A. Taniguchi, H. Okabe, H. Naito, N. Nakatsuka, and K. Oka, "Stabilized channeled spectropolarimeter using integrated calcite prisms," in *Polarization Science and Remote Sensing II,* vol. 5888 (International Society for Optics and Photonics, 2005), p. 588811.
45. T. Mu, S. Pacheco, Z. Chen, C. Zhang, and R. Liang, "Snapshot linear-stokes imaging spectropolarimeter using division-of-focal-plane polarimetry and integral field spectroscopy," Sci. reports **7**, 1–11 (2017).

National Science and Engineering Research Council of Canada (NSERC) Funding: STPGP 494358-16